Oxidation Resistance of TiAlN Coatings Deposited by Dual High-Power Impulse Magnetron Sputtering

**A. S. Grenadyorov[a], V. O. Oskirko[a], A. N. Zakharov[a], K. V. Oskomov[a],
V. A. Semenov[a], A. A. Solovyev[a], *, and A. N. Shmakov[b]**

[a] *Institute of High Current Electronics, Siberian Branch, Russian Academy of Sciences, Tomsk, 634055 Russia*
[b] *Budker Institute of Nuclear Physics, Siberian Branch, Russian Academy of Sciences, Novosibirsk, 630090 Russia*
*e-mail: andrewsol@mail.ru

Abstract—$Ti_{1-x}Al_xN$ coatings with different Al content ($x = 0.1-0.43$) are grown on WC–Co substrates by dual high-power impulse magnetron sputtering in the Ar/N_2 atmosphere. The coating resistance to high-temperature oxidation is determined. For this, the phase composition change is investigated by synchrotron radiation during heating in the air from room temperature to 1100°C. Mechanical properties (hardness, elastic modulus, plasticity index, and plastic deformation resistance) are determined by nanoindentation of coatings before and after heating to 1100°C. X-ray diffraction patterns demonstrate the formation of the TiO_2 phase on the surface of all coatings, while the formation temperature and the phase type (brookite or rutile) depend on the Al content in the coating. All coatings are not subject to spinodal decomposition into the TiN and AlN phases after heating to 1100°C. The $Ti_{0.57}Al_{0.43}N$ coating possesses the highest heat resistance; it undergoes the smallest change in the phase composition and mechanical properties after the high-temperature treatment.

INTRODUCTION

Due to the high hardness, wear and oxidation resistance, nitride coatings TiN, TiAlN, and CrAlN are often used in industry to increase the lifetime of cutting tools [1, 2]. Cutting tools operate under a complex group of factors including high contact stresses and temperature. Therefore, coatings should have high oxidation resistance in the temperature range of 800–1000°C. Lately, transition metal nitrides, in particular, TiAlN coatings have been considered excellent candidates for high-temperature solar absorbers [3–5]. Optical and electron properties of TiAlN coatings can vary in a wide range depending on the Al content [6]. According to [7–10], their main benefit lies in the stability of structure and properties under high-temperature annealing.

At a low Al content ($x \le 0.6$), the $Ti_{1-x}Al_xN$ coating is a face-centered cubic (FCC) substitutional solid solution in the TiN crystal lattice. At a higher Al content ($x > 0.7$), the wurtzite structure is more stable [11]. Within the range of 700–1000°C, the FCC $Ti_{1-x}Al_xN$ coating is subject to spinodal decomposition into FCC TiN and AlN phases [12, 13].

Greczynski et al. [14] distinguish several oxidation mechanisms of TiAlN coatings depending on the Al content.

In the case of Type-1 oxidation (at a low Al content), oxygen on the coating surface penetrates inside due to mostly vacancy diffusion and reacts mainly with titanium with the formation of the TiO_2 phase. Since Al solubility in the TiN and TiO_2 phases is restricted, released aluminum tends to diffuse on the surface where it oxidizes to Al_2O_3. In a deeper region, the lack of aluminum results in the formation of the TiO_2 phase. Therefore, both metals (aluminum and titanium) are well separated and react with oxygen at different depths, causing the formation of the two-layer structure Al_2O_3/TiO_2. The outer Al_2O_3 layer is very dense and provides surface passivation.

With an increasing Al content, oxidation is characterized by partial aluminum diffusion resulting in the formation of the aluminum gradient (transition mechanism). The oxide layer on the coating surface is a mixture of Al_2O_3/TiO_2.

At a high Al content (Type-2 oxidation), a balance between the surface oxidation rate and aluminum released from the lattice (after the reaction between Ti and O) is such that the aluminum gradient, as well as

Table 1. Parameters of the $Ti_{1-x}Al_xN$ coating deposition

Parameters	Stage 1 (ion cleaning and activation)	Stage 2 (TiAlN deposition)		
Ti magnetron power P_{Ti}, kW	1	1		
Ti magnetron discharge voltage, V	696 ± 5	696 ± 5		
Al magnetron power P_{Al}, kW	–	0.05	0.5	1
Al magnetron discharge voltage, V	–	632 ± 5		
Pulse duration τ, μs	20	20		
Frequency, kHz	5	5		
Substrate bias voltage U_b, V	−900 ± 10	−100 ± 5		
Ar flow rate, sccm	83 ± 1			
N_2 flow rate, sccm	–	12 ± 1		
Substrate temperature, °C	450 ± 10			
Process time, min	5	120		

its diffusion on the surface, does not appear. Once all titanium oxidizes, oxygen reacts with aluminum, thus, forming a mixed oxide layer Al_2O_3/TiO_2, which poorly passivates the surface. The TiO_2 layer is porous, and once it reaches a threshold thickness, it causes the coating spallation, hence, drastically reducing the oxidation resistance of the system [14].

Chavee et al. [10] showed that oxidation mechanisms of the $Ti_{1-x}Al_xN$ coating were similar to those of coatings deposited by different techniques, e.g., DC magnetron sputtering and high-power impulse magnetron sputtering (HiPIMS). Nevertheless, different techniques provide the formation of various structures and densities of coatings, which affect their oxidation resistance. For example, dense coatings ensure better oxidation resistance than columnar coatings or coatings with the droplet fraction on the surface formed by cathodic arc evaporation [15].

In this work, in situ investigations are conducted for the $Ti_{1-x}Al_xN$ coating structure obtained by dual short-pulse HiPIMS during continuous heating to 1100°C in the air. To the authors' knowledge, there is virtually no information offered in the literature concerning such investigations, and this work aims to fill this gap. The dual short-pulse HiPIMS system is used to eliminate the effect of disappearing anode observed in reactive deposition modes. HiPIMS provides higher ionization of the sputtered material, while ion energy can be controlled by substrate bias voltage.

In this work, the synchrotron radiation beam of the electron-positron storage ring is used to conduct in situ investigations of the structure and phase composition of the $Ti_{1-x}Al_xN$ coating with different Al content at a continuous temperature rise up to 1100°C.

The effect of the Al content on the oxidation resistance of the TiAlN coating is studied in this work.

EXPERIMENTAL

Coating Preparation

WC−Co (8 wt % Co, CNIC, China) alloy plates 10 × 10 × 3 mm in size were used as substrates. The surface of the plates was manually ground on 600# and 1200# diamond abrasive and polished on an MP-1B abrasive machine (TIME Group Inc., China) with a diamond paste grain size of 9 μm (Polylab, Russia). Prior to the coating deposition, the substrates were cleaned ultrasonically in isopropyl alcohol and acetone at 50°C. In each liquid, the substrates were treated for 10 min.

The $Ti_{1-x}Al_xN$ coating was deposited using the dual magnetron sputtering system with a 0.2 m³ vacuum chamber [16]. Al (99.95% purity), and Ti (99.95% purity) cathodes 76 mm in diameter were used for sputtering. The vacuum chamber was evacuated by a turbomolecular pump to a residual pressure of 8×10^{-3} Pa. The substrate temperature was 450°C during the coating deposition. The deposition process was conducted in a mixture of argon and nitrogen. Prior to the deposition process, the substrate surface was activated to improve the coating adhesive strength. The substrate bias voltage was $U_b = -900$ V, the frequency and pulse time were $f_b = 100$ kHz and $\tau_b = 4$ μs, respectively. The discharge power of the Al magnetron ranged between 0.05 and 1 kW to obtain the $Ti_{1-x}Al_xN$ coating with the different Al content. Table 1 summarizes the process parameters, the substrate bias voltage being −100 V.

Table 2. EDX results for the $Ti_{1-x}Al_xN$ coating

Samples	P_{Al}, kW	Ti, at %	Al, at %	N, at %	Ti/Al	Chemical composition
1	0.05	52.4 ± 1	5.9 ± 0.2	41.7 ± 4	8.9	$Ti_{0.9}Al_{0.1}N$
2	0.5	41.0 ± 0.8	18.5 ± 0.4	40.5 ± 4	2.2	$Ti_{0.69}Al_{0.31}N$
3	1	29.8 ± 0.6	22.2 ± 0.4	48.0 ± 5	1.3	$Ti_{0.57}Al_{0.43}N$

Table 3. Nanoindentation results for $Ti_{1-x}Al_xN$ coatings

Chemical composition	Thickness, μm	H, GPa	E, GPa	H/E	H^3/E^2, MPa
$Ti_{0.9}Al_{0.1}N$	1.5	28.1 ± 0.2	341.2 ± 0.5	0.082	190.6
$Ti_{0.69}Al_{0.31}N$	0.85	26.7 ± 0.2	304.5 ± 0.5	0.087	205.3
$Ti_{0.57}Al_{0.43}N$	1.75	27.5 ± 0.2	298.8 ± 0.5	0.092	232.9

Methods

Scanning electron microscopy (SEM) with the X-ray microanalysis of the elemental composition and surface morphology of the $Ti_{1-x}Al_xN$ coating was carried out using a Quanta 200 3D (FEI, USA) scanning electron microscope coupled with an energy-dispersive X-ray analyzer. The measurements were performed at acceleration voltage of 30 kV. The detected coating thickness ranged between 0.85 and 1.75 μm.

A NanoTest 600 hardness tester (Micro Materials Ltd., GB) was used to measure the $Ti_{1-x}Al_xN$ coating hardness and elastic modulus by the Oliver–Pharr method [17] at a load of 20 mN. The hardness testing was performed by a nanohardness indenter of a three-sided Berkovich pyramid shape.

The $Ti_{1-x}Al_xN$ coating structure and phase composition were investigated in the temperature range of 30 to 1100°C. The X-ray diffraction (XRD) analysis was conducted by using the synchrotron radiation beam of the VEPP-3 storage ring operating as part of the VEPP-4 Ion Collider Facility at the Budker Institute of Nuclear Physics SB RAS, Novosibirsk, Russia. The operating parameters included 0.172 nm radiation length, 10°C/min heating rate, 1 frame per minute exposure time, as well as 25 and 55° (2θ) scan range. The VEPP-4 is equipped with an HTK 2000 (Anton Paar) high-temperature chamber and an OD-3M-350 position sensitive detector. The Fityk 1.3.1 program was used for data processing. XRD patterns and their series are presented for Cu radiation (λ = 0.15406 nm) to compare them with the results of other authors.

RESULTS AND DISCUSSION

Table 2 presents the EDX results of the $Ti_{1-x}Al_xN$ coating compositions. As expected, the increase in the Al magnetron power produces a higher Al content in the coating and, consequently, a lower Ti/Al ratio.

In Fig. 1, SEM images show the surface and cross-section of the $Ti_{1-x}Al_xN$ coatings with different Al content. The surface is homogeneous, with small defects. The coating structure is dense and has good adhesion to the substrate.

According to Table 3, the increased Al content reduces the coating hardness and elastic modulus. The plasticity index H/E and plastic deformation resistance H^3/E^2 increase. The $Ti_{0.57}Al_{0.43}N$ coating possesses the highest H/E and H^3/E^2 values that may indicate high impact, wear, and crack resistance [18, 19]. Chavee et al. [10] report on the nanohardness of 29.1 ± 1.6 GPa of the $Ti_{0.58}Al_{0.42}N$ coating obtained by dual magnetron sputtering, whereas Greczynski et al. [20] produced the $Ti_{0.6}Al_{0.4}N$ coating with slightly lower hardness (24 GPa) when using Ti and Al target sputtering in DC and HiPIMS modes.

A slight hardness decrease with an increasing Al content in the $Ti_{1-x}Al_xN$ coating contradicts the results obtained by Liu et al. [21]. They observed the hardness growth from 23 to 31 GPa when the Al content (x) increased from 0 to 0.41. Liu et al. considered the hardness growth due to a change in the interatomic bonds resulting from Al interstitial atoms in the TiN lattice; grain-boundary strengthening (or Hall–Petch strengthening); and solid solution strengthening (Fleischer strengthening model). According to [21], at a higher ($x > 0.33$) and relatively low ($x \leq 0.33$) Al concentration, the most likely are grain-boundary strengthening and solid solution strengthening, respectively.

Synchrotron X-ray diffraction (XRD) patterns in Fig. 2 describe the initial $Ti_{0.9}Al_{0.1}N$ coating and that after heating to 1100°C with successive cooling down to room temperature. The as-deposited $Ti_{0.9}Al_{0.1}N$ coating structure is cubic and TiN-like with (111) preferred orientation. Due to the low ($x = 0.1$) Al content, the peak positions of the coating are close to those of the c-TiN phase (ICDD 00-038-1420), which is indicated with dashed lines in Fig. 2. In the initial coating, the TiN(111) peak shifts to the low-angle region due to compressive residual stresses typical for coatings
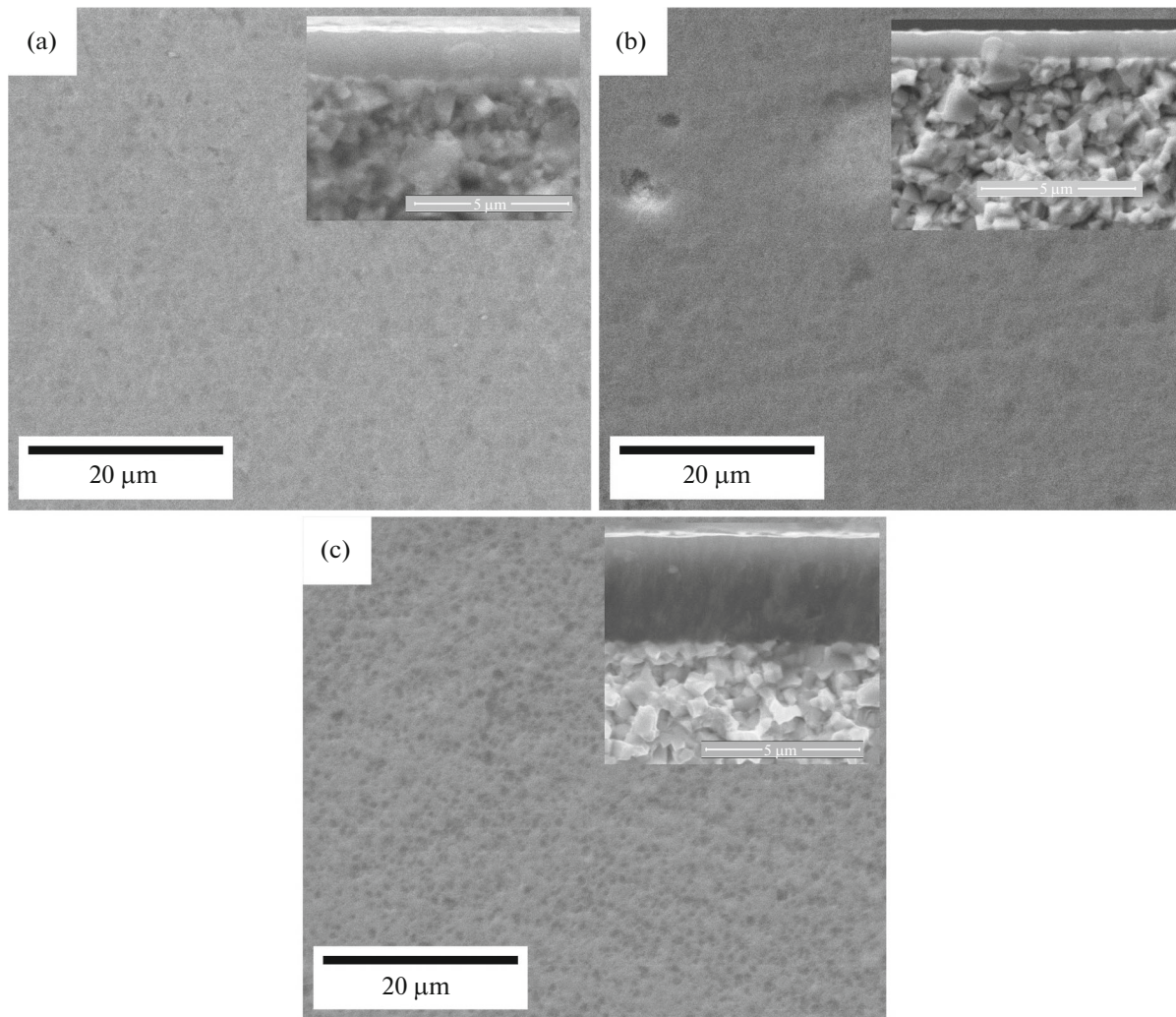
Fig. 1. SEM images of $Ti_{1-x}Al_xN$ coating surface with various Al content: (a) $Ti_{0.9}Al_{0.1}N$, (b) $Ti_{0.69}Al_{0.31}N$, (c) $Ti_{0.57}Al_{0.43}N$. Inserts: cross-section.

deposited by magnetron sputtering combined with substrate bias voltage. As compared to the tabulated value, the lattice parameter of the coating material increases by about 0.0022 nm. The spread-out TiN(200) peak is low-intense.

After the coating is heated and cooled down to room temperature, its structure contains a certain amount of the unoxidized TiN phase with the TiN(111) peak position matching the tabulated value of the lattice parameter. This indicates the relaxation of internal stresses in TiN grains. Rutile appears in the coating structure, which is an oxide mineral composed of titanium dioxide (TiO_2).

A series of XRD patterns of the $Ti_{0.9}Al_{0.1}N$ coating is presented in Fig. 3 as the intensity projection to the diffraction angle–time plane. During the heating up of the coating to 1100°C, the TiN(111) peak intensity drops at ~800°C. At the same time, one can see the peaks of the rutile phase, i.e., the coating starts to oxi-

dize. At 1100°C, the peak intensity of the coating reduces by almost 3 times, while the rutile peak intensity grows. During cooling, the coating phase composition remains unchanged.

In Fig. 4, XRD patterns demonstrate the $Ti_{0.69}Al_{0.31}N$ coating before and after heating to 1100°C followed by cooling down to room temperature. Despite the high ($x = 0.31$) Al content, the coating consists only of the TiN phase with (200) preferred orientation. The lattice parameter of the coating material is reduced by ~0.003 nm compared to the tabulated value, which may indicate aluminum incorporation into the TiN lattice.

In the final state (after heating to 1100°C and cooling to room temperature), the $Ti_{0.69}Al_{0.31}N$ coating consists of the TiO_2 (rutile and brookite) and TiN phases with the reduced lattice parameter and the Ti_3AlN phase.
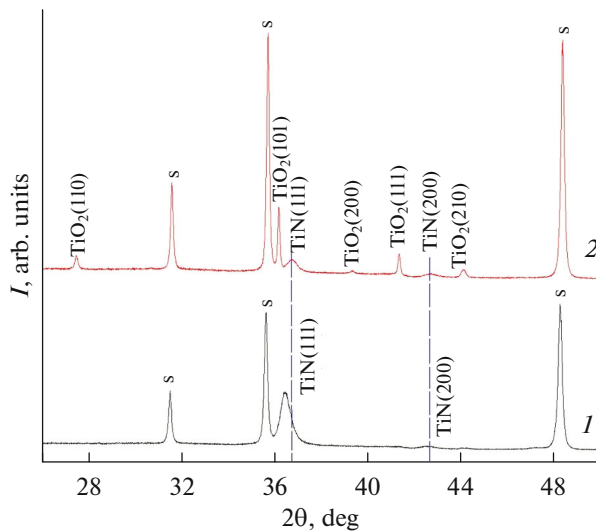
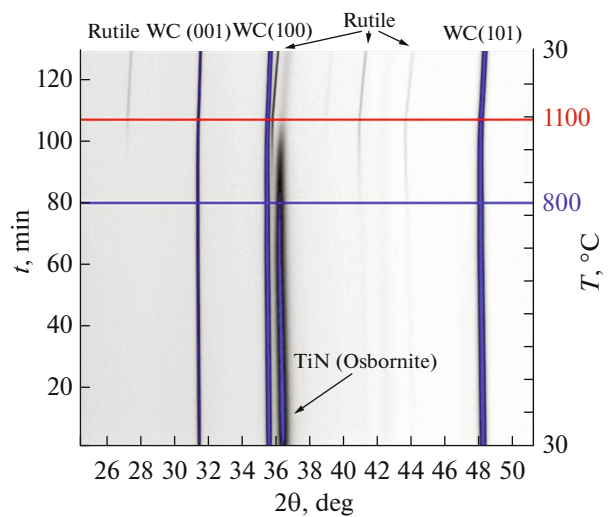**Fig. 2.** XRD patterns of the $Ti_{0.9}Al_{0.1}N$ coating before (spectrum *1*) and after (spectrum *2*) heating to 1100°C.

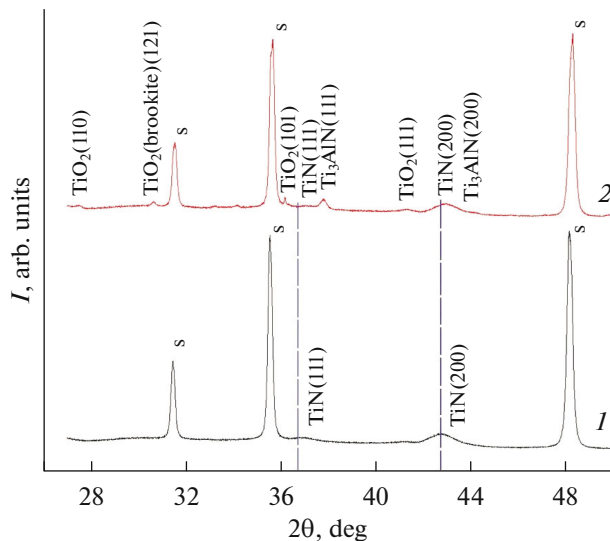**Fig. 3.** Series of XRD patterns of the $Ti_{0.9}Al_{0.1}N$ coating during heating to 1100°C in the air.

Fig. 4. XRD patterns of the $Ti_{0.69}Al_{0.31}N$ coating before (spectrum *1*) and after (spectrum *2*) heating to 1100°C.
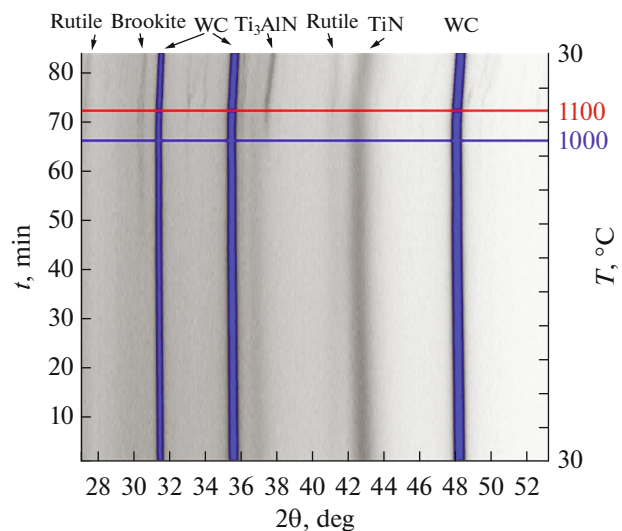

Fig. 5. Series of XRD patterns of the $Ti_{0.69}Al_{0.31}N$ coating during heating to 1100°C in the air.

According to Fig. 5, during heating of the $Ti_{0.69}Al_{0.31}N$ coating to 1100°C in the air, weak reflections are observed within ~840–850°C, which can be attributed to the brookite phase. In other words, this coating manifests higher oxidation resistance than the $Ti_{0.9}Al_{0.1}N$ coating due to the following factors. First, the phase composition changes at a temperature higher by 50°C; second, the peak intensity of the TiO_2 phase and, thus, its content in the coating is lower; and third, brookite is a nonequilibrium TiO_2 phase since, at the temperature rise, titanium dioxide modifies from anatase to rutile *via* brookite [22]. Moreover, the rutile and Ti_3AlN phases appear just at ~1000°C rather

than at 800°C, as in the case of the $Ti_{0.9}Al_{0.1}N$ coating. The peak intensity of the titanium nitride phase reduces, which indicates a decrease in its content in the coating.

XRD patterns in Fig. 6 describe the $Ti_{0.57}Al_{0.43}N$ coating composition before and after heating to 1100°C followed by cooling to room temperature. In the initial state, the cubic TiN and Ti_3AlN phases are detected in the coating composition. In this case, the peak intensity of titanium nitride is low; however, peaks do not shift relative to the tabulated values, although the synthesis conditions are nonequilibrium, as in previous cases. This is probably associated with
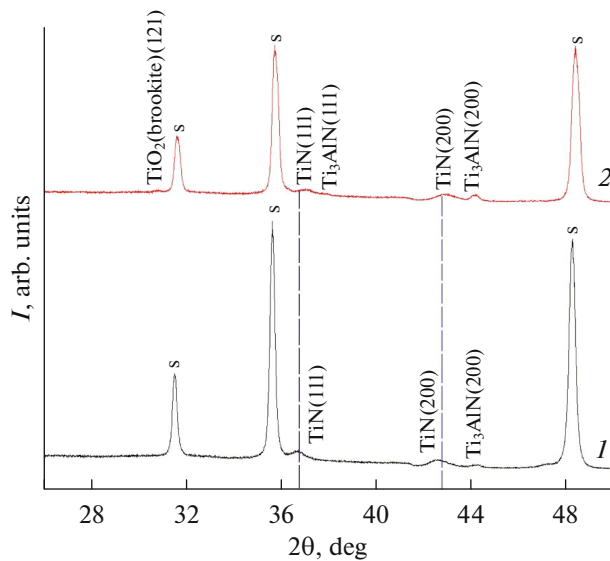
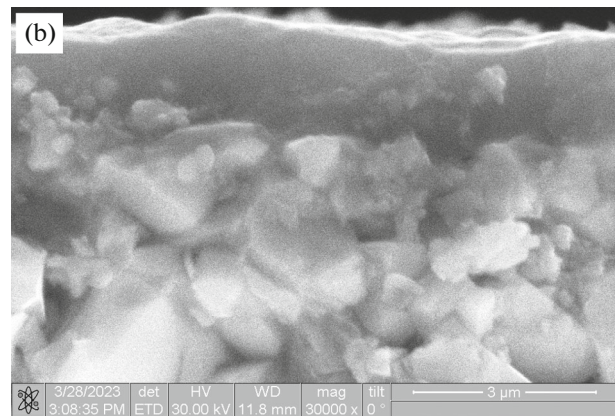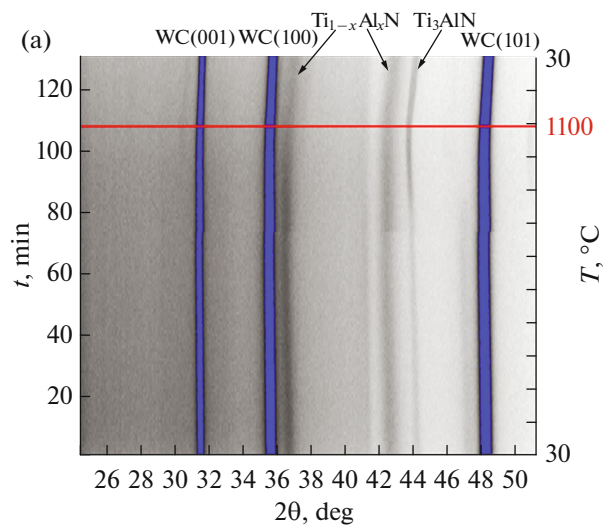**Fig. 6.** XRD patterns of the $Ti_{0.57}Al_{0.43}N$ coating before (spectrum *1*) and after (spectrum *2*) heating to 1100°C.

Fig. 7. Series of XRD patterns of the $Ti_{0.57}Al_{0.43}N$ coating during heating to 1100°C in the air (a), SEM image of the $Ti_{0.57}Al_{0.43}N$ coating after heating to 1100°C (b).

Al incorporation into the lattice of titanium nitride that reduces its parameter, thus, compensating for an increase in the lattice parameter of titanium nitride owing to nonequilibrium synthesis conditions and a disordered structure.

In the final state (after heating to 1100°C and cooling to room temperature), the $Ti_{0.57}Al_{0.43}N$ coating consists of the brookite and TiN phases with the reduced lattice parameter and the Ti_3AlN phase.

According to Fig. 7a, during heating of the $Ti_{0.57}Al_{0.43}N$ coating to 1100°C in the air, weak reflections of the brookite phase are observed at ~1000°C (the rutile phase is not detected). In other words, this coating is resistant to oxidation till this temperature point. At the same time, the peak intensity of the Ti_3AlN phase grows within ~820–850°C, while the TiN phase peaks shift to the large-angle region, manifesting a lattice parameter decrease due to the Al incorporation.

Table 4 presents $Ti_{1-x}Al_xN$ coating nanoindentation results after heating to 1100°C in the air. As can be seen from this table, all mechanical properties get worse. This is because the maximum temperature in our experiment is higher than allowable (800–900°C)

for this coating type [23, 24]. Nevertheless, an increase in the Al content in the coating leads to lower degradation of its mechanical properties after the high-temperature treatment. The $Ti_{0.9}Al_{0.1}N$ and $Ti_{0.57}Al_{0.43}N$ coatings show a 79 and 47% decrease in the hardness, respectively. This means that the $Ti_{0.57}Al_{0.43}N$ coating is more resistant to high-temperature treatment.

According to the XRD analysis, the $Ti_{0.9}Al_{0.1}N$ coating with a lower Al content contains the rutile phase already after heating to 800°C in the air. As for the $Ti_{0.57}Al_{0.43}N$ coating with the highest Al content,

Table 4. $Ti_{1-x}Al_xN$ coating indentation results after heating to 1100°C in the air

Chemical composition	H, GPa	E, GPa	H/E	H^3/E^2, MPa
$Ti_{0.9}Al_{0.1}N$	5.9 ± 0.1	225.2 ± 0.4	0.026	4.1
$Ti_{0.69}Al_{0.31}N$	8.2 ± 0.1	199.7 ± 0.4	0.041	13.8
$Ti_{0.57}Al_{0.43}N$	14.7 ± 0.2	374.4 ± 0.5	0.039	22.8

the brookite phase occurs only under heating to 1000°C, while the rutile phase is not observed at all.

The phase and chemical compositions of the coatings correlate with each other. Spacing between the TiN lattice planes reduces with an increasing Al content; this indicates Al atom incorporation into the TiN crystal lattice, which substitutes Ti atoms. The formation of the Ti_3AlN phase is observed already in the initial $Ti_{0.57}Al_{0.43}N$ coating and in the $Ti_{0.69}Al_{0.31}N$ coating after heating to 1000°C. It is worth noting that none of the investigated coatings contains either cubic or hexagonal (wurtzite) AlN phase, i.e., no spinodal decomposition of the FCC $Ti_{1-x}Al_xN$ coating occurs, as opposed to [10, 12, 13]. This is probably associated with relatively fast coating heating without the high-temperature exposure for hours resulting in a lack of time for lattice atom diffusion, which induces the formation of c-AlN- and c-TiN-enriched domains due to spinodal decomposition.

As is known, spinodal decomposition and w-AlN phase formation depended not only on the temperature of annealing but also on its duration. Rachbauer et al. [12] studied the $Ti_{0.46}Al_{0.54}N$ coating deposited by DC magnetron sputtering. They observed spinodal decomposition at 800°C during 2-hour annealing, whereas 1-min annealing at 1000°C was enough for spinodal decomposition. Interestingly, the Al_2O_3 phase did not appear after annealing but was observed in [8, 25] after the high-temperature annealing of the $Ti_{1-x}Al_xN$ coating. That was probably associated with a relatively low Al content in the coatings.

Figure 7b shows the SEM image of the cross-section of the $Ti_{0.57}Al_{0.43}N$ coating after its heating to 1100°C. One can see that the coating structure is preserved rather dense without well-defined columnar grains typical for coatings deposited by magnetron sputtering. There are no porous structures or delaminations of the coating that can be caused by a great difference between the molar volumes of the TiN and TiO_2 phases [14].

CONCLUSIONS

The research has concerned the influence of the Al content on the mechanical properties and heat resistance of the $Ti_{1-x}Al_xN$ coating ($x = 0.1-0.43$) synthesized using dual high-power impulse magnetron sputtering from two single-component Ti and Al targets. The heat resistance was investigated by the X-ray diffraction method and the synchrotron radiation during the heating of the coated WC−Co substrate in the air from room temperature to 1100°C. It was shown that the Al content did not strongly modify the coating hardness ranging between 26 and 28 GPa. However, at the maximum ($x = 0.43$) Al content, the $Ti_{1-x}Al_xN$ coating demonstrated the highest plasticity index ($H/E = 0.092$) and plastic deformation resistance ($H^3/E^2 = 232.9$ MPa).

The as-deposited $Ti_{0.9}Al_{0.1}N$ coating with the minimum Al content possessed a cubic TiN-like structure with (111) preferred orientation. This coating started to oxidize under heating to ~800°C in the air, which was proven by the diffraction peaks of the rutile phase. When the annealing temperature was raised to 1100°C, the TiN phase reflection was reduced by almost 3 times, while the peak intensity of the rutile phase increased. The initial $Ti_{0.57}Al_{0.43}N$ coating with the highest Al content comprised the cubic TiN and Ti_3AlN phases. Under heating to ~1000°C, the XRD patterns showed weak reflections of the brookite phase, while the rutile phase was not observed. Therefore, the increase in the Al content in the coating significantly exceeded its oxidation resistance. That was also proven by a change in the coating hardness after heating to 1100°C, i.e., the hardness of the $Ti_{0.9}Al_{0.1}N$ coating was 5.9 GPa, and that of the $Ti_{0.57}Al_{0.43}N$ coating was 14.7 GPa.

CONFLICT OF INTEREST

The authors of this work declare that they have no conflicts of interest.

REFERENCES

1. P. J. Kelly, T. von Braucke, Z. Liu, R. D. Arnell, and E. D. Doyle, Surf. Coat. Technol. **202**, 774 (2007). https://doi.org./10.1016/j.surfcoat.2007.07.047

2. L. Aihua, D. Jianxin, C. Haibing, C. Yangyang, and Z. Jun, Int. J. Refract. Met. Hard Mater. **31**, 82 (2012). https://doi.org/10.1016/j.ijrmhm.2011.09.010

3. K. Ibrahim, H. Taha, M. M. Rahman, H. Kabir, and Z.-T. Jiang, J. Opt. **20**, 033001 (2018). https://doi.org/10.1088/2040-8986/aaa2c5

4. L. Xiong, Y. Liu, Z. He, X. Shao, D. Gong, B. Yang, H. Liu, X. Hu, and K. Liu, Vacuum **197**, 110836 (2022). https://doi.org/10.1016/j.vacuum.2021.110836

5. J. Feng, S. Zhang, Y. Lu, H. Yu, L. Kang, X. Wang, Z. Liu, H. Ding, Y. Tian, and J. Ouyang, Sol. Energy **111**, 350 (2015). https://doi.org/10.1016/j.solener.2014.11.005

6. S. Kassavetis, G. Abadias, G. Vourlias, G. Bantsis, S. Logothetidis, and P. Patsalas, Surf. Coat. Technol.

295, 125 (2016).
https://doi.org/10.1016/j.surfcoat.2015.08.049

7. B. Breidenstein, N. Vogel, H. Behrens, M. Dietrich, and J. M. Andersson, J. Surf. Investig. **16**, 663 (2022).
https://doi.org/10.1134/S1027451022040231

8. G. Biava, I.B.A. F. Siqueira, R. F. Vaz, G.B. de Souza, H.C. M. Jambo, A. Szogyenyi, and A.G. M. Pukasiewicz, Surf. Coat. Technol. **438**, 128398 (2022).
https://doi.org./10.1016/j.surfcoat.2022.128398

9. S. Das, S. Guha, R. Ghadai, and B. P. Swain, Mater. Chem. Phys. **258**, 123866 (2021).
https://doi.org./10.1016/j.matchemphys.2020.123866

10. L. Chavee, E. Serag, M. S. Pires, S. Lucas, and E. Haye, Appl. Surf. Sci. **586**, 152851 (2022).
https://doi.org./10.1016/j.apsusc.2022.152851

11. A. Kimura, H. Hasegawa, K. Yamada, and T. Suzuki, Surf. Coat. Technol. **120-121**, 438 (1999).
https://doi.org./10.1016/s0257-8972(99)00491-0

12. R. Rachbauer, J. J. Gengler, A. A. Voevodin, K. Resch, and P. H. Mayrhofer, Acta Mater. **60**, 2091 (2012).
https://doi.org/10.1016/j.actamat.2012.01.005

13. B. Grossmann, M. Tkadletz, N. Schalk, C. Czettl, M. Pohler, and C. Mitterer, Surf. Coat. Technol. **342**, 190 (2018).
https://doi.org/10.1016/j.surfcoat.2018.02.062

14. G. Greczynski, L. Hultman, and M. Odén, Surf. Coat. Technol. **374**, 923 (2019).
https://doi.org/10.1016/j.surfcoat.2019.06.081

15. M. Tkadletz, C. Mitterer, B. Sartory, I. Letofsky-Papst, C. Czettl, and C. Michotte, Surf. Coat. Technol. **257**, 95 (2014).
https://doi.org/10.1016/j.surfcoat.2014.01.010

16. A. Grenadyorov, V. Oskirko, A. Zakharov, K. Oskomov, and A. Solovyev, Materials **15**, 8237 (2022).
https://doi.org/10.3390/ma15228237

17. W.C. Oliver and G. M. Pharr, J. Mater. Res. **19**, 3 (2004).
https://doi.org/10.1557/jmr.2004.0002

18. J. L. Mo, M. H. Zhu, A. Leyland, and A. Matthews, Surf. Coat. Technol. **215**, 170 (2013).
https://doi.org/10.1016/j.surfcoat.2012.08.077

19. F. W. Zok and A. Miserez, Acta Mater. **55**, 6365 (2007).
https://doi.org/10.1016/j.actamat.2007.07.042

20. G. Greczynski, J. Lu, J. Jensen, S. Bolz, W. Kolker, Ch. Schiffers, O. Lemmer, J. E. Greene, and L. Hultman, Surf. Coat. Technol. **257**, 15 (2014).
https://doi.org/10.1016/j.surfcoat.2014.01.055

21. Z.-J. Liu, P. W. Shum, and Y. G. Shen, Thin Solid Films **468**, 161 (2004).
https://doi.org/10.1016/j.tsf.2004.05.087

22. A. Di Paola, M. Bellardita, and L. Palmisano, Catalysts **3**, 36 (2013).
https://doi.org/10.3390/catal3010036

23. A. O. Volkhonskii, I. V. Blinkov, Yu. V. Levinskii, and D. S. Belov, Russ. Metall. (Metally) **2018**, 1088 (2018).
https://doi.org/10.1134/S0036029518110125

24. G. Hao, Z. Liu, X. Liang, and J. Zhao, Coatings **9**, 355 (2019).
https://doi.org/10.3390/coatings9060355

25. P. Li, L. Chen, S. Q. Wang, B. Yang, Y. Du, J. Li, and M. J. Wu, Int. J. Refract. Met. Hard Mater. **40**, 51 (2013).
https://doi.org/10.1016/j.ijrmhm.2013.01.020